Revised direct radiative forcing of airborne microplastics suggests warming

Felix W. Goddard

felix.goddard@pg.canterbury.ac.nz

University of Canterbury

Stefania Glukhova

MacDiarmid Institute for Advanced Materials and Nanotechnology

Eric C. Le Ru

MacDiarmid Institute for Advanced Materials and Nanotechnology

Nikolaos Evangeliou

NILU

Cameron McErlich

University of Canterbury

Catherine Hardacre

University of Canterbury

David Frame

University of Canterbury

Peter Kuma

Swedish Meteorological and Hydrological Institute

Laura E. Revell

University of Canterbury

Article

Keywords:

Posted Date: June 30th, 2026

DOI: https://doi.org/10.21203/rs.3.rs-10121818/v1

Additional Declarations: No competing interests reported.

Revised direct radiative forcing of airborne microplastics suggests warming

Felix W. Goddard[1,*], Stefania Glukhova[2], Eric C. Le Ru[2], Nikolaos Evangeliou[3], Cameron McErlich[1], Catherine Hardacre[1], David Frame[1], Peter Kuma[4], and Laura E. Revell[1,*]

[1]School of Physical and Chemical Sciences, University of Canterbury, Christchurch, New Zealand
[2]The MacDiarmid Institute for Advanced Materials and Nanotechnology, School of Chemical and Physical Sciences, Victoria University of Wellington, Wellington, New Zealand
[3]Stiftelsen NILU (formerly NILU - Norwegian Institute for Air Research), Department for Atmospheric & Climate Research (ATMOS), 2007 Kjeller, Norway
[4]Rossby Centre, Swedish Meteorological and Hydrological Institute, Norrköping, Sweden
*Corresponding authors: felix.goddard@pg.canterbury.ac.nz and laura.revell@canterbury.ac.nz

Abstract

Microplastics are a common airborne pollutant, capable of being transported over large distances and with potential to alter the radiative properties of the atmosphere in large enough quantities, with implications for global climate. Since the first estimates of microplastic radiative forcing were published in 2021, new constraints on many aspects of the spatial and temporal distribution of airborne plastics and their physical and optical properties have emerged. Using these updated findings concerning the size distribution of airborne microplastics, new spectral absorption data for coloured plastics, and a new microplastic emissions dataset, we investigate the sensitivity of the direct radiative effect of airborne microplastics. We find clear-sky effective radiative forcings ranging from -3.28 to $+46.7$ mW m^{-2} depending on assumptions concerning colour, size distribution, vertical profile and spatial distribution. Assuming likely real-world conditions — a mix of coloured microplastics, a power law size distribution, and distributing microplastics non-uniformly through the troposphere based on a new emissions dataset — we calculate an updated estimate of $+42.1 \pm 4.62$ mW m^{-2} for a global-average surface concentration of 3.99 microplastics m^{-3}. This revised radiative forcing is at least as large in forcing magnitude as the contributions of a number of other species routinely evaluated by the Intergovernmental Panel on Climate Change. Our findings suggest that microplastics are likely contributing to atmospheric warming, and given that plastic pollution is projected to increase, should be included in climate change projections.

1 Main

In the past decade, microplastics (MPs, plastic particles < 5 mm in diameter) have emerged as a ubiquitous pollutant in the atmosphere, both close to major MP emission sources and in remote locations alike[1,2]. MPs are emitted from a wide variety of primarily urban sources and, once in the atmosphere, undergo long-range transport[3,4,5]. The atmospheric burden of microplastics is projected to increase over time as the amount of plastic waste in the environment increases, given the absence of fast or effective removal pathways[6]. Alongside concerns over their human health effects[7], MPs have potential to act as a short-lived climate forcer similar to other atmospheric aerosols. Aerosols impact the Earth's climate by altering the passage of radiation through the atmosphere. This may occur by direct interactions between aerosol particles and radiation (the direct radiative effect) and by interactions between aerosols and clouds, which alter cloud albedo, extent, and lifetime (the indirect radiative effect[8,9]). Recent work has demonstrated that MPs may impact cloud properties by acting as ice nucleating particles[10,11,12,13], and lower the surface albedo of snow and ice, accelerating melt rates[14,15].

Revell et al.[16] (hereafter R21) made the first estimate of the direct radiative effect of airborne MPs. They calculated a top-of-atmosphere effective radiative forcing (ERF; see Section 4.1) of $+0.044 \pm 0.399$ mW m^{-2} for non-pigmented MPs assuming a gamma distribution of particle sizes, a uniform surface concentration of 1 MP m^{-3} and a vertical distribution up to 10 km altitude. Fibers were shown to have a larger ERF than fragments due to their size and shape. When confined to the lowest 2 km of the atmosphere, the microplastic ERF was -0.746 ± 0.553 mW m^{-2}. The assumptions used by R21 were a necessity due to the scarcity of data available at the time, but are significant simplifications that do not represent reality, evidenced by more recent studies. Yang et al.[17] and Pang et al.[18] present estimates of the MP direct radiative effect using more realistic (i.e. spatially varying) surface concentrations. Yang et al.[17] modelled an urban area in which high concentrations of MPs had been measured, finding a highly variable radiative forcing that was correlated with atmospheric and land surface conditions. Pang et al.[18] performed global atmospheric transport simulations and calculated a global net top-of-atmosphere (TOA) radiative forcing of -6.34 µW m^{-2}, a net cooling in agreement with R21 but considerably smaller in magnitude. Liu et al.[19] used measurements of coloured plastics to show that pigmentation leads to increased absorption of solar radiation, and a shortwave radiative forcing of $+6$ mW m^{-2} for microplastics following the same size distribution used by R21. However, they did not model longwave effects.

Here we provide an exploration of the parameter space and an updated estimate of the direct radiative effect of airborne microplastics informed by new data. We perform sensitivity simulations with the same models used by R21 to identify the variables to which microplastic ERF is most sensitive, varying four factors that are key to determining the MP radiative effect: (1) MP colour, aided by new optical property data for coloured plastic polymers (as coloured microplastics are ubiquitous in the atmosphere[5,20,21]); (2) the MP size distribution, following literature analysis by Leusch et al.[22]; (3) the vertical extent of MP occurrence, informed by atmospheric transport studies[23,24,25]; and (4) the horizontal distribution of surface MP concentration, using new MP emissions data[3]. The simulations and models used are described in more detail in Section 4.

2 Results and discussion

To isolate the impact of each of the aforementioned parameters on the MP direct radiative effect, we perform seven global circulation model simulations: a reference simulation replicating the result of R21, five one-at-a-time tests with different parameter values, and a final 'Updated estimate' simulation that combines the parameter settings of the individual tests. Table 1 shows the scaled ERFs and instantaneous radiative forcings (IRFs, which unlike ERFs do not include the radiative impact of rapid adjustments; see Section 4.1) for each simulation; the simulation parameters are given in Table 2 and described in Sections 4.2–4.3.

Our net ERFs span a range from -3.28 to $+46.7$ mW m^{-2}, with the bulk of this spread due to differences between the parameter settings of simulations rather than the uncertainty of individual simulations. Our uncertainties are determined only by interannual variability in the circulation model — each simulation is run with a prescribed spatial distribution and optical properties, hence do not provide an estimate of parameter uncertainty. Our confidence intervals thus verify a statistically significant difference between parameter settings and demonstrate how radiative forcing is impacted by variations in that parameter.

Our net IRFs are generally only slightly greater in magnitude than the corresponding net ERFs, with a difference < 3 mW m^{-2} indicative of rapid adjustments having a weak moderating influence on the radiative forcing.

Fig. 1 shows the radiative forcing efficiency for each simulation, i.e. the radiative forcing per unit total MP mass burden. Our forcing efficiencies are relatively small, all < 10 mW m^{-2} Tg^{-1} in magnitude, compared to e.g. -363 ± 139 mW m^{-2} Tg^{-1} for sulfate aerosol[26]. This is likely due to the larger average size of MPs in our simulations, around 5 to 20 µm in diameter (Fig.

Table 1: Effective radiative forcing (ERF) derived from HadGEM3-GA7.1 simulations (defined in Table 2) and instantaneous radiative forcing (IRF) derived from analogous simulations with the SOCRATES radiative transfer model (Section 4.1). Uncertainties for ERFs are the 5 to 95% confidence interval of the distribution of forcing values over the 20 simulation years, assumed to follow a *t*-distribution. Radiative forcings are scaled to a global-average surface concentration of 3.99 MP m^{-3} between 50 and 100 µm diameter, following Leusch et al. [22].

	Simulation name	ERF (mW m^{-2})			IRF (mW m^{-2})			Total plastic burden (Tg) [b]
		SW	LW	Net	SW	LW	Net	
1	Previous estimate	-3.72 ± 0.40	$+1.18 \pm 0.57$	-2.55 ± 0.73	-4.77	$+1.79$	-2.97	0.92
2	Mixed-colour	-0.45 ± 0.10	$+1.06 \pm 0.16$	$+0.61 \pm 0.15$	-1.13	$+1.77$	$+0.64$	0.92
3	TBWP [a]	$+3.41 \pm 0.77$	$+0.36 \pm 1.19$	$+3.77 \pm 1.13$	$+4.47$	$+1.25$	$+5.72$ [c]	0.92
4	Power law size distribution	-4.67 ± 0.62	$+3.01 \pm 0.59$	-1.66 ± 0.65	-6.28	$+3.32$	-2.96 [c]	1.00
5	Whole troposphere	-18.1 ± 0.19	$+27.0 \pm 0.27$	$+8.88 \pm 0.27$	-25.6	$+28.4$	$+2.76$ [c]	4.28
6	Horizontally non-uniform	-2.70 ± 0.27	$+1.19 \pm 0.27$	-1.51 ± 0.41	-3.63	$+1.97$	-1.66	0.91
7	Updated estimate	-3.47 ± 3.38	$+45.5 \pm 4.51$	$+42.1 \pm 4.62$	-0.52	$+47.11$	$+46.6$	4.69

[a] Simulation 'TBWP' is named for tire- and brake-wear particles (TBWP; Section 4.2.3).
[b] Total plastic burdens were calculated by integrating the MP number concentration over the globe, following the spatial distributions described in Section 2.4, and converting particle number to mass using the average particle volume of the assumed size distribution and an average plastic density of 1.1 g cm^{-3}.
[c] Net IRF does not fall within the 5 to 95% confidence interval of the corresponding net ERF.

2), compared to fine-mode sulfate aerosol at around 0.1 µm [27,28,29]. Smaller particles produce a stronger forcing efficiency due to their greater number concentration for the same total mass (Section 2.2), and the Mie scattering efficiency is greatest for particles with a comparable size to the wavelength (0.2–10 µm in the shortwave spectrum).

With the 'Previous estimate' simulation we repeat the result of R21 for microplastics confined to the boundary layer. We note that their simulation used a 1:1 mixture of fibers and fragments whereas our simulations include only MP fragments (see Section 4.2.1). Scaling our ERF result (Table 1) to match their surface MP concentration (1 MP m^{-3}), we compute a radiative forcing of -0.094 ± 0.023 mW m^{-2} compared to their value of -0.746 ± 0.553 mW m^{-2}. Our result is smaller in magnitude and the confidence intervals do not quite overlap, though the discrepancy between the edges of the confidence intervals is small (-0.073 mW m^{-2}) and likely due to the absence of MP fibers in our simulations (see Section 4.2.1), which R21 demonstrated produce a stronger radiative forcing than fragments.

2.1 Effect of colour on MP radiative forcing

The effects of varying MP colour are shown in Fig. 1b–c (simulations 'Mixed-colour' and 'TBWP'), i.e. the calculated radiative forcing for MPs consisting of UV-absorbing mixed-colour plastic, and of UV-absorbing colourless plastic mixed with 20% black carbon (BC) by weight respectively.

The 'Mixed-colour' simulation (Fig. 1b) shows a shortwave cooling effect only 24% as large as that of the 'Previous estimate' simulation, owing to the warming effect of the absorption of solar radiation, due to the greater absorption cross-section of coloured plastic in the shortwave spectrum (Fig. 3). The shortwave effect is reduced enough that the net ERF efficiency is positive ($+0.67 \pm 0.17$ mW m^{-2} Tg^{-1}), indicating a net warming effect. The net ERF efficiency is,

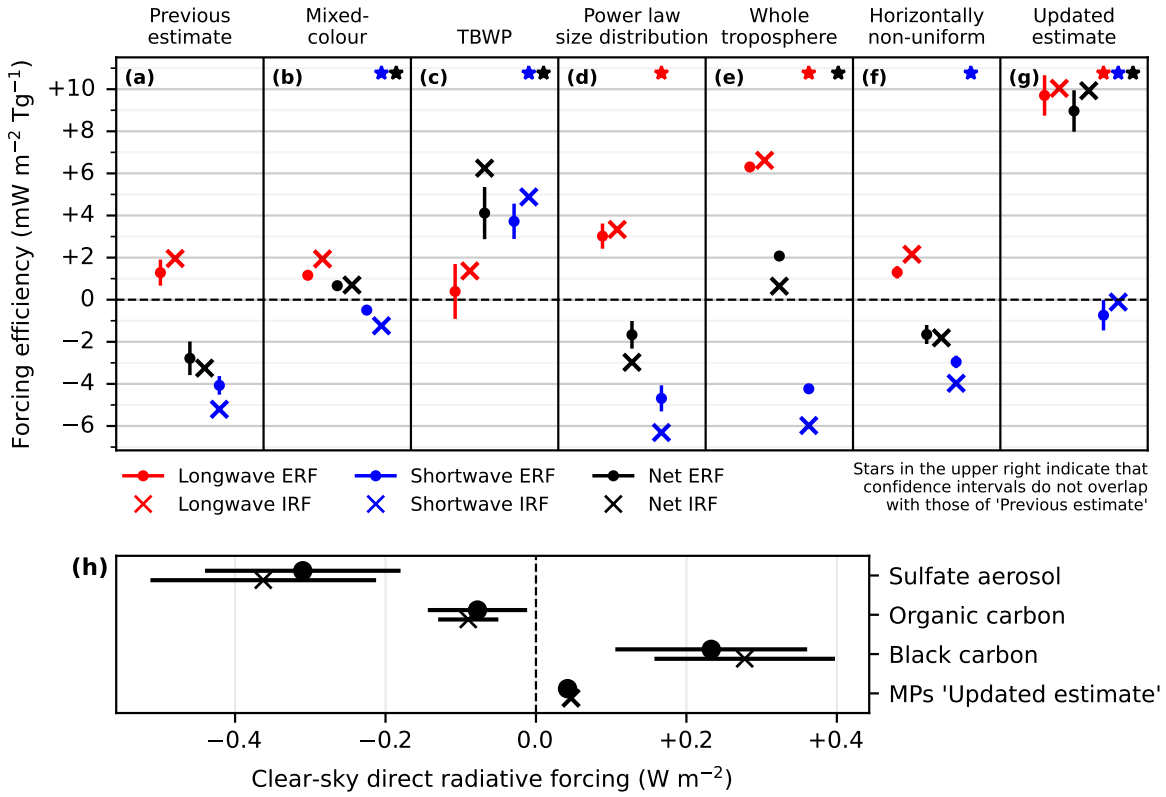

Figure 1: (a–g) Radiative forcing efficiency of microplastics (radiative forcing [mW m^{-2}] per unit total mass burden of MPs [Tg]) for each of our simulations (see Table 2 for details on simulation parameters). Red and blue symbols indicate the longwave and shortwave components of the forcing respectively; black symbols indicate the net forcing. Crosses indicate IRF efficiencies. Dots indicate ERF efficiencies, with bars indicating the 5 to 95% confidence interval of the 20 simulation years. Red, blue, and black stars in the upper right of each subplot indicate, for that simulation, that the confidence interval of the corresponding ERF component (longwave, shortwave, or net respectively) does not overlap with that of the 'Previous estimate' simulation (i.e. it is distinct in a statistically significant sense); note that simulations shown in panels (b)–(f) are one-at-a-time tests relative to 'Previous estimate'. (h) Comparison of current best-estimate aerosol clear-sky net radiative forcing (ERF_{ari} and IRF_{ari}) and 'Updated estimate' MP radiative forcing calculated in this study. Note that IRF estimates have error bars only for non-MP species. ERF_{ari} for non-MP species was calculated as the sum of IRF_{ari} and non-cloud rapid adjustments provided by Thornhill et al.[30]; uncertainty estimates are displayed here as half the inter-model range over the four models for which the relevant data were available.

however, much smaller in magnitude than the 'Previous estimate' experiment as the short- and longwave components are close to compensating each other.

Studies have demonstrated a wide variety of colours presented by airborne MPs (e.g., reviews by Mbachu et al.[20], Shao et al.[21]), and the UV-absorption we model here is a measured property of the plastic polymer itself (Section 4.2.3), hence our mixed-colour optical properties are more representative of typical plastic. In measurements of coloured MPs, Liu et al.[19] also found an increase in the shortwave absorption cross-section due to pigmentation. Environmental aging and the diversity of both colorant and non-colourant additives used in plastic production[31] may introduce further variation in the full-spectrum scattering and absorption properties of plastic particles, highlighting the need for studies characterising the spectral properties of MPs in the environment. Until such studies are available, we consider the optical properties used in the 'Mixed-colour' simulation to best represent reality and recommend them for use in future radiative transfer modelling of airborne MPs.

The 'TBWP' simulation (Fig. 1c) clearly shows the impact of the increased absorption cross-section of BC-containing plastic (Fig. 3). The shortwave forcing efficiency has a similar magnitude to that of the 'Previous estimate' but is instead positive, resulting in a positive net forcing (i.e. net warming). This change in the net forcing is attributable solely to the absorption of shortwave radiation, as the longwave forcing efficiency is not significantly different from that of the 'Previous estimate' experiment. The net ERF efficiency of this simulation is small, ($+4.12 \pm 1.24$ mW m^{-2} Tg^{-1}) compared to that of black carbon from fossil fuel and biofuel burning ($+2819 \pm 1235$ mW m^{-2} Tg^{-1}) but of the same order of magnitude as that of organic carbon and black carbon from biomass burning ($+14 \pm 310$ mW m^{-2} Tg^{-1})[26].

Plastic particles mixed with black carbon are known to be present in the atmosphere as tire and brake-wear particles (TBWP) and may undergo atmospheric transport over significant distances[32,3]. We also see higher forcing efficiencies over land areas with a higher surface albedo (Supplementary Fig. S1) where emissions inventories indicate the greatest emissions of TBWP from road traffic are found[3]. The discovery of black rubber particles in snow and the significant mass that TBWP may contribute relative to the mass of black carbon emissions suggests that TBWP in addition to black carbon may play a substantial role in snow albedo changes and the consequent acceleration of snow and ice melt[14,33,34,35]. The distinct warming properties of TBWP seen here compared to other MP particles (represented by the 'Previous estimate' experiment) therefore highlights the important role they may play in the overall MP radiative forcing.

2.2 Effect of size distribution on MP radiative forcing

The impact of a power law size distribution on the MP radiative forcing efficiency is shown in Fig. 1d (simulation 'Power law size distribution'). The longwave ERF efficiency for this experiment (3.02 ± 0.60 mW m^{-2} Tg^{-1}) is 2.3× greater than that of the 'Previous estimate', likely due to the higher concentration of larger particles, with the power law size distribution resulting in more particles at radii > 35 µm than the gamma size distribution (Fig. 2). These larger particles interact more strongly with longwave radiation; this can be seen in the smaller reduction in scattering cross sections at the long wavelength end of the spectrum compared to the spectra of gamma size distributed particles (Fig. 3).

In a literature analysis by Leusch et al.[22], a power law size distribution was found to be a good fit to MP size distributions across a range of environmental compartments, and a power law distribution is expected on theoretical grounds due to the fractal nature of particle fragmentation[36,37].

We set the lower bound of our size distributions at 1 µm diameter as this is close to the smallest particle size at which current analytical techniques can reliably measure particle number concentrations[38]. Smaller plastic particles, i.e. nanoplastics, are known to exist in the environment and their mass concentrations are beginning to be characterised (e.g. Materić et al.[39]).

Nanoplastics may remain suspended in the atmosphere for longer, undergo greater horizontal and vertical transport, and are more numerous at the same mass concentrations, amplifying their forcing efficiencies (Supplementary Fig. S2). A recent study showed that the IRF of airborne nanoplastics could be several times larger than the corresponding IRF for microplastics[19]. However, these calculations should be considered preliminary because analytical methods for quantifying nanoplastics are still under development. In particular, the nanoplastic size distributions used to inform Liu et al.[19]'s calculations were measured by pyrolysis-gas chromatography/mass spectrometry (py-GC/MS), which frequently identifies false positives, leading to measured nanoplastic concentrations 10× higher than the more established thermal desorption-proton transfer reaction-mass spectrometry (TD-PTR-MS) method[40]. Future research should revisit nanoplastic radiative forcing once reliable global estimates of nanoplastic abundances and size distributions are available.

2.3 Effect of vertical distribution on MP radiative forcing

The effect of distributing MPs vertically throughout the whole troposphere is shown in Fig. 1e (simulation 'Whole troposphere'). The net ERF efficiency of this simulation (+2.07±0.06 mW m^{-2} Tg^{-1}) is positive due to a substantial (5×) increase in the longwave forcing efficiency (+6.31±0.06 mW m^{-2} Tg^{-1}) relative to that of the 'Previous estimate' (+1.29 ± 0.62 mW m^{-2} Tg^{-1}).

R21 also found a stronger radiative forcing when including MPs up to 10 km altitude than when confined to the lowest 2 km. Our 'whole troposphere' vertical distribution (see Section 4.3) extends to the tropopause, up to 17 km altitude near the equator. Samset and Myhre[41] show that the black carbon forcing efficiency increases with altitude, such that a large proportion of the total BC forcing is contributed by BC at high altitude. We replicate this result in Supplementary Fig. S3, which shows that the efficiency of longwave forcing increases with altitude such that a strong warming effect is contributed by high-altitude MPs. This suggests that the increase in longwave efficiency of our 'Whole troposphere' simulation is governed largely by the increase in total vertical extent of MPs.

Measurements and model studies of the vertical distribution of aerosols show that, subject to variations due to local conditions, aerosols are generally present above the boundary layer with concentrations decaying exponentially with height[42,43,44,45]. Transport modeling studies for airborne MPs have shown that MPs can be mixed throughout the troposphere, and may be transported into the stratosphere in limited amounts[23,24,25] (see also Fig. 4a). Tatsii et al.[23] show that particle shape can have a significant influence on the distance and altitude to which microplastics can be transported, with fiber morphotypes being dispersed further and higher due to their lower settling velocities. These findings suggest that our whole-troposphere vertical distribution provides a better approximation to the vertical extent of MPs than the 'Previous estimate' experiment, which has no MPs above 2 km altitude.

2.4 Effect of horizontal distribution on MP radiative forcing

The effect of a non-uniform MP surface concentration is shown in Fig. 1f. This simulation ('Horizontally non-uniform') produces a shortwave ERF efficiency 27% smaller in magnitude than that of the 'Previous estimate' simulation. This reduced shortwave cooling is due to the reduction in MP concentration over the open ocean, where surface albedo is low and scattering aerosols like (non BC-containing) MPs have a stronger cooling effect. Supplementary Fig. S1d shows the difference in the distribution of total MP burden across surfaces of varying albedo. Surfaces with an albedo < 0.08, over which colourless MPs have the strongest cooling effect, account for all ice-free ocean and underlie 62% of the total MP burden in the 'Previous estimate' simulation but only 18% in the 'Horizontally non-uniform' simulation.

Major airborne MP sources — synthetic textiles, tire and brake wear, industrial activity, landfill, waste incineration, and degradation of macroplastics in the environment — are pri-

marily terrestrial[1,46,21]. Macroplastics degrade to produce microplastics in the marine environment[47,48] and marine MPs can be emitted into the atmosphere[49,50,51], however MP number concentrations over the ocean are low[5,52] and the ocean is likely not a significant source of airborne MPs compared to the land surface[53,54,55,56]. This suggests that, even though the precise horizontal distribution of MP concentrations is poorly constrained by the observational evidence, the qualitative impact of the land–ocean contrast on the MP radiative effect that we find in our simulations is accurate.

2.5 Updated estimate of MP radiative forcing

The 'Updated estimate' simulation is shown in Fig. 1h, i.e. the combined effect of assuming mixed-colour plastic, a power law size distribution, a whole-troposphere vertical distribution, and a non-uniform horizontal distribution. As discussed in Sections 2.1–2.4, the parameter choices of this simulation provide a more realistic approximation of the real-world properties and distribution of airborne MPs than those of the 'Previous estimate'. This result therefore offers the most reliable estimate of the MP direct radiative forcing currently available in the literature, but excludes nanoplastic and TBWP radiative forcing as comparatively little is known about airborne nanoplastics and TBWPs have a very distinct spectral absorption cross-section.

The impact of each individual parameter choice can be seen in the 'Updated estimate' simulation. The shortwave forcing efficiency is reduced to near-zero (-0.74 ± 0.72 mW m^{-2} Tg^{-1}), as seen in simulations 'Mixed-colour', due to absorption in the shortwave spectrum, and 'Horizontally non-uniform', where reduction in MP concentrations over the oceans weakens the shortwave cooling effect. The longwave forcing efficiency ($+9.70 \pm 0.96$ mW m^{-2} Tg^{-1}) is considerably greater than the 'Previous estimate' simulation, as seen in simulations 'Power law size distribution', due to the relative increase in the concentration of larger particles, and 'Whole troposphere', due to the greater vertical extent of MPs. The combination of a weakened shortwave cooling and an amplified longwave warming results in the net ERF efficiency of this simulation being the most positive (warming) of any of our simulations ($+8.97 \pm 0.99$ mW m^{-2} Tg^{-1}). This is in contrast to the net negative (cooling) effect of the 'Previous estimate' simulation, and the cooling effects found by Revell et al.[16] and Pang et al.[18]. Liu et al.[19] also found a net warming due to MPs, however their work neglected the longwave effect which we demonstrate is a large component of the overall MP ERF.

Considering comparable measures of radiative forcing for other aerosol species (i.e. clear-sky net ERFs and IRFs reported by Thornhill et al.[30]), shown in Fig. 1i, our new estimate of the MP radiative effect is small in comparison to that of other aerosol species, being e.g. 17% the magnitude of the black carbon ERF. Additionally, uncertainties in the aerosol radiative forcing arising from differences between models are large (even in absence of cloud-aerosol interactions, which introduce further uncertainty) and are not represented in our estimates which are produced with a single set of related models.

3 Discussion and outlook

In this work we investigate a range of variations on the optical properties and spatial distribution of airborne MPs, isolating the impact of these parameter variations on direct radiative forcing. Our sensitivity simulations yield an ERF ranging from -3.28 to $+46.7$ mW m^{-2}, and an ERF efficiency ranging from -3.58 to $+9.95$ mW m^{-2} Tg^{-1}, showing how these parameters can substantially impact the calculated radiative forcing.

At present, the paucity of quantitative constraints on parameter values preclude a true estimate of parameter uncertainty, however our results give what we suggest is a viable range for the microplastic ERF (-3.28 to $+46.7$ mW m^{-2}) and what we consider to be a most probable subset of that range ($+42.0 \pm 4.62$ mW m^{-2}, given by our 'Updated estimate'). We also emphasise the parameters which produce the greatest breadth in this viable range — the absorption

cross-section in the shortwave spectrum, and the maximum altitude at which MPs are found — as areas on which future research should be focused.

The 'Updated estimate' simulation provides, to our knowledge, the most accurate assessment of the direct radiative forcing of airborne microplastics to date. Combining various lines of evidence to inform the most likely settings for each of the parameters considered, we obtain a radiative forcing efficiency of 8.97±0.99 mW m^{-2} Tg^{-1} (yielding a net ERF of +42.0±4.62 mW m^{-2} at an atmospheric plastic burden of 4.69 Tg). In contrast to the negative radiative forcing found by Revell et al.[16], Pang et al.[18], and in agreement with Liu et al.[19], this indicates that airborne MPs contribute overall to atmospheric warming via their direct radiative effect. TBWP additionally form a substantial portion of the real atmospheric MP burden, over 50% in some countries[57], and contribute a warming effect in our 'TBWP' simulation which is not included in our 'Updated estimate'.

Evangelou et al.[56] recently identified that most microplastics inventories overestimate emissions. The non-uniform surface concentration of airborne MPs assumed in this study is lower in the global-mean than that reported by Evangelou et al.[56] (3.99 cf. their 31 MP m^{-3}), but higher in the median (0.34 cf. their 0.03 MP m^{-3}). Taking into account the different particle size ranges used (1–100 µm cf. their 5–100 µm) and scaling our 'Updated estimate' experiment to a median surface MP concentration matching that of their compiled observations yields an ERF of +9.74 mW m^{-2}. Either way, the range from this to our 'Updated estimate' ERF (+42.0 mW m^{-2}) would place microplastics above most of the anthropogenic forcers assessed by the Intergovernmental Panel on Climate Change (IPCC), of which around half have ERFs of 1 mW m^{-2} in magnitude or smaller[58].

MPs do not undergo rapid permanent removal from circulation in the total environment by any natural process, and may have extremely long residence times in numerous environmental compartments[6]. However, estimating future climate forcing is difficult due to multiple large uncertainties. Stegmann et al.[59] model annual plastic waste production under a moderate future greenhouse gas emissions scenario, projecting a total waste plastic mass 10.1× greater than in 2023 by 2100. As a rough approximation, extrapolating our 'Updated estimate' to a 10.1× greater surface concentration yields a radiative forcing of +425 ± 47 mW m^{-2}. We acknowledge the very large uncertainties in plastic waste projections, rates of plastic degradation to produce microplastics, and the airborne fraction of the global microplastic burden (e.g. the role of the ocean as a sink or reservoir for microplastics[2]). Nonetheless, a direct radiative forcing of $\sim$ +0.43 W m^{-2} would be significant — larger than other aerosol species currently assessed by the IPCC (Fig. 1h).

Overall, we have illustrated the crucial role that uncertainties in microplastic optical properties, spatial distribution, and total abundance play in ERF estimates, highlighting the essential role of improved observation of the characteristics of microplastics in the environment. It seems clear that microplastics are overdue to be included as forcings in future climate change assessments, justifying more widespread attention towards this forcing source from the climate research, and perhaps policy, community.

4 Computational methods

4.1 Modelling of radiative effects

The radiative effects of atmospheric species such as aerosols or trace gases are quantified through metrics such as the effective radiative forcing (ERF) and instantaneous radiative forcing (IRF), which comprise the change in top-of-atmosphere (TOA) radiative balance due to the perturbing species and varying degrees of atmospheric adjustment[60,61]. IRF is evaluated without allowing the atmospheric column to change, so does not include the radiative effects of so-called rapid adjustments, whereas ERF allows properties of the atmospheric column such as the temperature and moisture to change in response to the forcing on short timescales. Rapid adjustments

are not coupled to the change in global-average surface air temperature and so do not constitute climate feedbacks[62,63]. ERF can be determined from the relationship between radiative forcing and feedback:

$$\Delta N = \mathrm{ERF} - \lambda \Delta T \tag{1}$$

where ΔN, λ, and ΔT represent the TOA energy imbalance (W m^{-2}), the climate feedback parameter (W m^{-2} K^{-1}), and the change in global surface air temperature respectively (K).

Here we present estimates only of the ERF due to aerosol-radiation interactions ($\mathrm{ERF_{ari}}$, henceforth simply ERF). MPs may have impacts on cloud formation[11,10,12,64,13] and hence a component of their ERF may be due to aerosol-cloud interactions (i.e. $\mathrm{ERF_{aci}}$). However, the model version used for this study is not configured to represent microplastic-cloud interactions and we focus only on direct radiative effects.

Estimates of the MP ERF were calculated from simulations using the Hadley Centre Global Environment Model version 3–Global Atmosphere model 7.1 (HadGEM3-GA7.1), developed by the UK Met Office and Momentum Partnership[65]. The model uses a regular 1.25° × 1.875° latitude-longitude grid with 85 unevenly-spaced vertical levels between the surface and 85 km altitude. The model radiative transfer scheme uses the Suite of Community Radiative Transfer codes based on Edwards and Slingo (SOCRATES; Edwards and Slingo[66]). As configured in HadGEM3-GA7.1, the shortwave part of the spectrum between 200 nm and 10 µm is divided into six spectral bands and the longwave part between 3.3 µm and 1 cm into nine spectral bands. Sea surface temperatures (SSTs) and sea-ice concentrations were prescribed from the Hadley Centre Global Sea Ice and Sea Surface Temperature observational dataset[67]. Greenhouse gas concentrations and aerosol emissions follow CMIP6 recommendations[68]. Each experiment was run for 21 years, from Sep 1988 to Sep 2009 and the first year of simulation was discarded as spin-up.

Following R21, we introduce airborne MPs in HadGEM3-GA7.1 using the non-interactive aerosol scheme (EasyAerosol), which enables the prescription of user-defined spatial distributions of aerosol species within the model. These aerosols interact only with radiation and are provided to the model as absorption and scattering coefficients on model grid cells and levels, hence they do not undergo interactive transport, emission or deposition, or microphysical processing. This configuration avoids making additional assumptions about microplastic properties such as settling velocities, scavenging coefficients, emission and resuspension rates, etc. MP optical properties were averaged across the model spectral bands, weighted in the shortwave by the incoming solar spectrum[69], and multiplied by the prescribed MP number concentration to convert to volume absorption and scattering coefficients.

ERFs are calculated as the change in the global-mean TOA clear-sky outgoing radiation relative to a control simulation which was run with no microplastics[61]. As SSTs in both simulations are prescribed, the surface air temperature response is suppressed and the change in TOA radiative balance approximates the ERF (equivalent to setting $\Delta T = 0$ in Equation 1). ERF is calculated separately for the shortwave and longwave components:

$$\mathrm{ERF_{SW}} = \uparrow \mathrm{SW_{Perturbed}} - \uparrow \mathrm{SW_{Control}} \tag{2}$$

$$\mathrm{ERF_{LW}} = \uparrow \mathrm{LW_{Perturbed}} - \uparrow \mathrm{LW_{Control}} \tag{3}$$

$$\mathrm{ERF_{Net}} = \mathrm{ERF_{SW}} + \mathrm{ERF_{LW}} \tag{4}$$

where $\uparrow$ denotes the global-mean TOA clear-sky outgoing radiation flux.

Top-of-atmosphere radiative fluxes were calculated as global annual means of the daily mean time series. We assume each 20-year time series of ERF estimates $\boldsymbol{X}$ is t-distributed with $N - 1 = 19$ degrees of freedom, mean $\overline{\boldsymbol{X}}$, and scale $\sqrt{\mathrm{Var}[\boldsymbol{X}]/N}$ where $\mathrm{Var}[\boldsymbol{X}]$ denotes the variance of $\boldsymbol{X}$. The 5% to 95% confidence interval for the mean ERF was calculated from this t-distribution.

To estimate IRF, we employ the radiative transfer model SOCRATES which calculates

radiative fluxes for a given atmospheric structure. Unlike HadGEM3-GA7.1, SOCRATES simulates no dynamics or physics processes, hence the atmosphere is held constant and no rapid adjustments can occur. For each latitude and longitude of the global HadGEM3-GA7.1 grid, we use annual-mean profiles of air temperature, moisture, ozone, and surface shortwave albedo calculated from ERA5 reanalyses[70]. Surface longwave emissivity was set to a constant value of 1. Fluxes were estimated using the two-stream approximation with a latitudinally-varying annual-mean daytime solar zenith angle. As the atmosphere is held constant for IRF calculations, no time series of annual IRFs are available from which to derive a confidence interval. As such we report only the global-mean IRF with no uncertainty.

We consider seven different experiments, detailed in Table 2, consisting of different combinations of optical properties (Section 4.2) and prescribed spatio-temporal distribution (Section 4.3). As in R21, we exaggerate the global-average surface MP concentration of each experiment in order to achieve a clear signal-to-noise ratio in the radiative forcing, and then scale the resultant IRF and ERF down to correspond to a realistic observationally-constrained global-average surface MP concentration, assuming that the MP radiative effect is proportional to the global-average surface MP concentration, i.e.

$$\mathrm{RF}_{\mathrm{scaled}} = \mathrm{RF}_{\mathrm{simulated}} \times \frac{[\mathrm{MP}]_{\mathrm{scaled}}}{[\mathrm{MP}]_{\mathrm{simulated}}} \tag{5}$$

where [MP] denotes the global-average surface MP concentration and $[\mathrm{MP}]_{\mathrm{scaled}} = 3.99$ MP m^{-3} between 50 and 100 µm diameter; note that we consider MPs ranging from 1 to 100 µm diameter, hence $[\mathrm{MP}]_{\mathrm{scaled}}$ is equivalent, over the full range of particle sizes, to a total number concentration of 27.3 MP m^{-3} and 91.7 MP m^{-3} for the gamma and power law size distributions respectively (see Section 4.2.2). Due to the different forcing efficiencies of each experiment, each required a different choice of $[\mathrm{MP}]_{\mathrm{simulated}}$ to achieve the same signal-to-noise ratio, hence for each experiment we prescribe a different global-average surface MP concentration (Table 2). Example calculations and further explanation of the scaling procedure are given in Supplementary Text S4.

We report the radiative effect as both a global-average radiative forcing (mW m^{-2}; listed in Table 1) and as a forcing efficiency (mW m^{-2} Tg^{-1}; shown in Fig. 1). The forcing efficiency is defined as the global-average radiative forcing per unit total mass burden of forcer. To calculate MP particle mass we assume a plastic density of 1.1 g cm^{-3}.

4.2 Microplastic optical properties

4.2.1 Morphotype

MPs in the environment are classified according to their morphotype as fragments, fibers, or films. R21 considered fragments and fibers, neglecting films due to their lesser prevalence and a lack of information about their size distribution. Here we assume that all MPs are in the form of fragments, neglecting fibers due to the complexity in calculating their optical properties, requiring additional assumptions about fiber size and shape, and because R21 already quantified the effect of morphotype on the MP radiative forcing. Their results for fragments and fibers found ERFs of -18.3 ± 62.5 and -38.8 ± 52.0 mW m^{-2} respectively.

We assume fragments are approximately spherical, allowing for the calculation of their absorption and scattering cross sections and asymmetry factors using Mie theory, following the methodology of R21.

4.2.2 Size distribution

The distribution of the diameter of MP fragments in R21 was given by a gamma distribution with shape parameter 2 and scale parameter 15 µm determined by fitting to the limited obser-

Table 2: Names and parameters of the seven simulations carried out. All simulations were run for 21 years from 1 Sep 1988 with the first year discarded as spin-up. Global-average surface number concentrations prescribed in the horizontal distribution were increased in order to attain a clear signal-to-noise ratio in the ERF. Reported results have been scaled down to correspond to a global-average surface MP number concentration of 3.99 MP m^{-3} between 50 and 100 µm diameter (see Section 4.2.2).

	Simulation name	Colour	Size distribution	Vertical distribution	Horizontal distribution [a]
1	Previous estimate	colourless [b]	gamma [c]	confined to < 2 km [e]	uniform, 1680 MP m^{-3}
2	Mixed-colour	mixed-colour [b]	gamma	confined to < 2 km	uniform, 7230 MP m^{-3}
2	TBWP	BC-containing [b]	gamma	confined to < 2 km	uniform, 860 MP m^{-3}
4	Power law size distribution	colourless	power law [d]	confined to < 2 km	uniform, 5710 MP m^{-3}
5	Whole troposphere	colourless	gamma	whole troposphere [f]	uniform, 2620 MP m^{-3}
6	Horizontally non-uniform	colourless	gamma	confined to < 2 km	non-uniform, 3070 MP m^{-3}
7	Updated estimate	mixed-colour	power law	whole troposphere	non-uniform, 650 MP m^{-3}

[a] Listed concentrations denote prescribed global-average surface MP number concentrations, corresponding to $[MP]_{simulated}$ in Equation (5).
[b] Absorption and scattering cross-sections for colourless, mixed-colour, and BC-containing plastics are shown in Fig. 3a, 3b, and 3c respectively.
[c] Gamma size distribution is given by Equation (6).
[d] Power law size distribution is given by Equation (7).
[e] 'Confined to < 2 km' vertical distribution is given by Equation (10).
[f] 'Whole troposphere' vertical distribution function is given by Equation (11).

vations available at that time (Equation 6). Following Leusch et al.[22] we also consider a power law size distribution (Equation 7).

$$\frac{\mathrm{d}N}{\mathrm{d}r} = A\left(\frac{2r}{15}\right)^2 \frac{1}{r} e^{-2r/15} \tag{6}$$

$$\frac{\mathrm{d}N}{\mathrm{d}r} = Br^{-\alpha} \tag{7}$$

where r is the particle radius in µm, $N(r)$ gives the number of particles in a bin of particle radius $(r, r + \mathrm{d}r)$, A and B (particles m^{-3} µm^{-1}) are normalisation constants that determine the total particle number concentration, and α determines the shape of the power law distribution. For both size distributions, we consider only MPs between 1 and 100 µm diameter (i.e. 0.5 µm $\leq r \leq$ 50 µm, assuming a spherical shape).

Based on Leusch et al.[22], we set $B = 36.6$ MP m^{-3} µm^{-1} and $\alpha = 1.52$ for outdoor airborne MPs. With these parameters, the power law predicts a MP number concentration of 3.99 MP m^{-3} in a bin of particle diameter from 50 to 100 µm (chosen as good observational data is available for such a size range). We match the gamma distribution to the number concentration in this range by choosing $A = 27.6$ MP m^{-3} µm^{-1} (i.e. such that $\int_{25\ \mu\mathrm{m}}^{50\ \mu\mathrm{m}} \frac{\mathrm{d}N}{\mathrm{d}r}\,\mathrm{d}r =$ 3.99 MP m^{-3} for both distributions). Over the full range of particle sizes (1 to 100 µm diameter) this is equivalent to a total number concentration of 27.3 MP m^{-3} and 91.7 MP m^{-3} for the gamma and power law size distributions respectively. We use these particle number concentrations when scaling radiative forcings to realistic surface concentrations.

The two size distributions are shown in Fig. 2. Particle cross sections scale with the particle area, which is 3.5× greater for the gamma size distribution than for the power law size distribution. Particle number concentrations scale inversely with the particle volume (when holding total mass constant), which is 3.1× greater for the gamma size distribution than for the power law size distribution.

4.2.3 Refractive index

Only colourless MP particles were considered by R21, modelled by a polynomial fit to available measurements of the refractive indices of various plastic polymers. We present two alternatives to this: UV-absorbing mixed-colour plastic, accounting for observed absorption in the UV-visible spectrum that was neglected in R21; and BC-containing plastic, as an approximation to tire- and brake-wear particles (TBWP; Evangeliou et al.[3]). In both these cases, we account for the optical absorption using the complex refractive index, $m = n + ik$.

To determine the full-spectrum complex refractive index of a colourless UV-absorbing plastic polymer, we combined measurements of the refractive index of a UV-absorbing clear plastic for wavelengths $<$ 400 nm, the refractive index of the clear (non UV-absorbing) polymer from R21 for wavelengths $>$ 400 nm, and the complex refractive index of PET in the UV range from Ouchi[71]. BC-containing plastic was modelled as this clear plastic with black carbon spheres mixed homogeneously throughout.

For coloured plastics, we first measured the transmission $T(\lambda)$ of coloured PET plastic films of known thickness L. The imaginary part of the refractive index can then be deduced from Equation 8.

$$k = \frac{2.303\lambda}{4\pi L}\left[-\log_{10} T(\lambda)\right] \tag{8}$$

To determine the effect of pigments on the real part of the refractive index, the results were then fitted to Kramers-Kronig-consistent functions[72], in our case Lorentzian oscillators, and then combined with the refractive index of a clear UV-absorbing polymer. Diffuse reflectance spectroscopy measurements were also performed to confirm that the results were consistent with

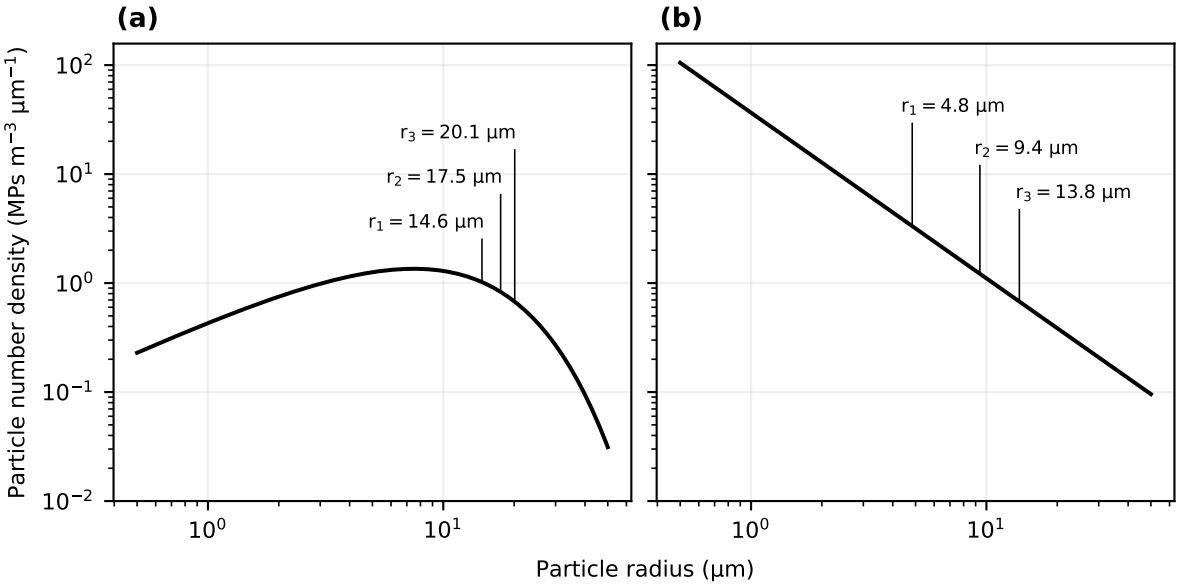

Figure 2: (a) Gamma and (b) power law MP size distributions considered in this work. Both distributions are defined over 0.5 to 50 µm radius and are normalised to have the same total particle number concentration within the range 25 to 50 µm radius. Vertical tick marks and text indicate the average particle radius (r_1) and the effective radii of the area- and volume-average particles (r_2 and r_3 respectively) for the two distributions.

reflection measurements and independent of scattering. The full results will be presented in a separate publication. The resultant refractive indices are shown in Supplementary Fig. S5. The mixed-coloured plastic was modelled as an equal mixture of four dye colours of plastic samples (blue, indigo, pink, and red). The peak in the imaginary part in the visible range corresponds to the dye absorption. The amplitude of this peak in practice depends on the actual concentration of the colourants; here we use a typical concentration for coloured plastics.

For each set of refractive indices, we calculate the scattering and absorption spectra using Mie theory and average across the range of particle sizes weighted by the size distribution (see Section 4.2.3), viz.:

$$\overline{\sigma}(\lambda) = \frac{\int \sigma(r,\lambda)\,\mathrm{d}N}{\int \mathrm{d}N} = \frac{\int_{r_{\min}}^{r_{\max}} \sigma(r,\lambda)\frac{\mathrm{d}N}{\mathrm{d}r}\,\mathrm{d}r}{\int_{r_{\min}}^{r_{\max}} \frac{\mathrm{d}N}{\mathrm{d}r}\,\mathrm{d}r} \tag{9}$$

where $\sigma(r,\lambda)$ denotes the Mie scattering or absorption cross-section of a particle of radius r at wavelength λ, and $\overline{\sigma}(\lambda)$ denotes the size-average spectrum.

Fig. 3 shows the absorption and scattering spectra for each combination of refractive indices and particle size distribution. Strong absorption peaks in the UV and visible spectrum are clearly seen in Fig. 3b–c due to the UV-absorption and presence of pigments. The addition of black carbon (Fig. 3d) results in a substantial increase in absorption across the whole spectrum. The power law size distribution gives smaller cross sections than the gamma size distribution due to the smaller average particle cross-sectional area. This affects scattering and absorption approximately equally, resulting in a largely unchanged single-scattering albedo. For both size distributions the asymmetry factor approaches zero as wavelength increases, reflecting the Rayleigh limit ($\lambda \gg r$), however the power law size distribution is closer to this limit at smaller wavelengths due to the smaller particle size, hence the asymmetry factor is smaller (i.e. more isotropic scattering) across much of the spectrum.

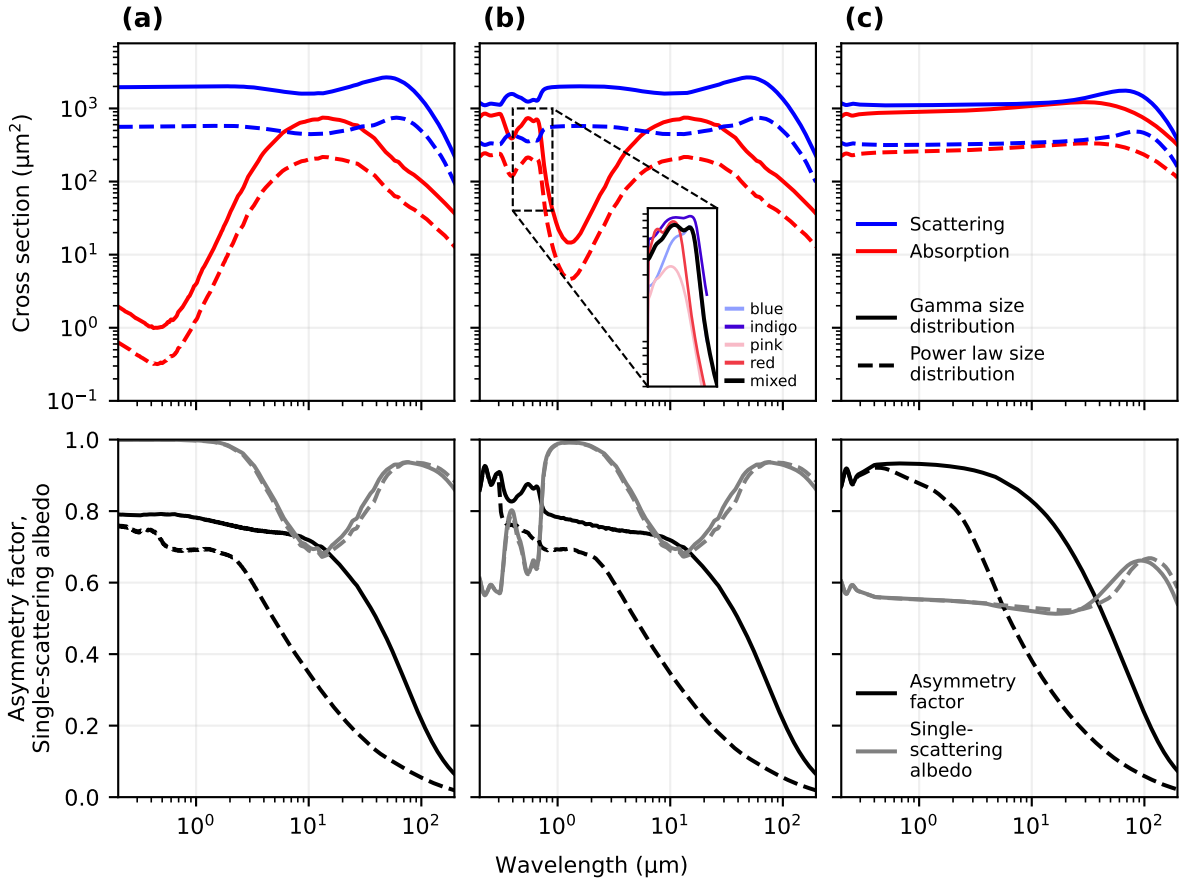

Figure 3: Absorption and scattering cross sections (top row) and asymmetry factor and single-scattering albedo (bottom row) for microplastic spheres of varying composition: (a) colourless plastic, (b) UV-absorbing mixed-colour plastic, (c) UV-absorbing colourless plastic mixed with 20% black carbon by weight. Solid lines indicate properties for particles following a gamma size distribution; dashed lines follow a power law size distribution. The inset plot in panel (b) shows the absorption spectra of the four constituent colours that make up the mixed-colour plastic, following the gamma size distribution.

4.3 Spatio-temporal distribution of microplastics

We separate the spatio-temporal distribution of microplastics into a horizontally-varying surface concentration, denoted ρ_0, and a vertical distribution that describes how the MP concentration declines from the surface concentration in the vertical direction.

For the surface MP concentration ρ_0, R21 considered a constant value which we also use here and denote by "uniform". We additionally consider a spatially-varying ρ_0, derived from a particle transport simulation using FLEXPART and the MP emissions dataset of Evangeliou et al. [73], with subsequent updates to ocean emissions to better account for the distribution of microplastics in surface waters per Isobe et al. [74]. The spatially-varying ρ_0 we consider here (denoted by "non-uniform" and used in experiments 'Horizontally non-uniform' and 'Updated estimate') was taken from the time-average surface MP concentration of this simulation and is shown in Fig. 4b.

The vertical distribution of MPs in R21 was given by Equation 10, which decreases the concentration of MPs approximately in accordance with the decrease in air density with increas-

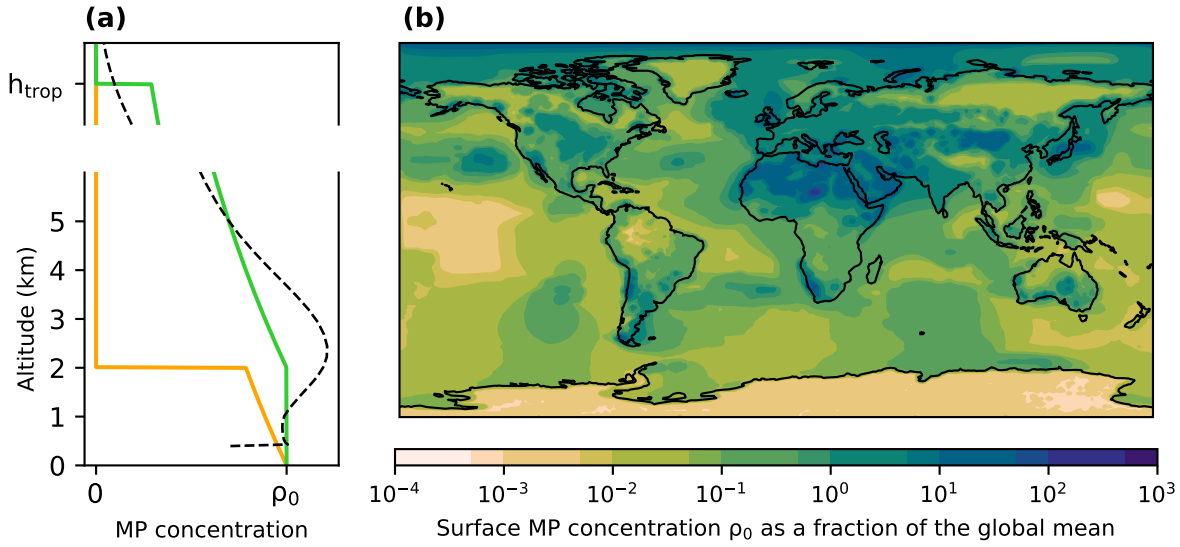

Figure 4: (a) Microplastic vertical distribution functions 'confined to $<$ 2 km' (orange line, Equation (10)) and 'whole troposphere' (green line, Equation (11)). Dashed line shows the distribution of MP fragments $>$ 1 µm in diameter in McErlich et al.[25]. (b) Surface microplastic concentration given by the non-uniform distribution, as a fraction of the global-average surface concentration.

ing altitude. The MP concentration is set to zero above a cutoff altitude z_{cutoff}. R21 considered both $z_{\text{cutoff}} = 10$ km and $z_{\text{cutoff}} = 2$ km, approximating the tropopause and boundary layer height respectively. We consider this vertical distribution with $z_{\text{cutoff}} = 2$ km, as a more conservative base case for the 'Previous estimate' simulation, and denote this distribution by 'confined to $<$ 2 km'.

$$\rho(z) = \rho_0 \times \begin{cases} 0.3^{z/10\text{ km}} & z \le z_{\text{cutoff}} \\ 0 & z > z_{\text{cutoff}} \end{cases} \tag{10}$$

We consider an alternative vertical distribution (Equation 11) as a closer approximation to real-world conditions, particularly the impact of MP vertical transport. This distribution has a constant MP concentration from the surface up to an altitude z_{BL}, above which the MP concentration decreases like air density up to the tropopause. Above the tropopause the MP concentration is zero. This distribution is intended to approximate an average vertical distribution of aerosols in the real atmosphere (e.g. Xiang et al.[75], Sheridan et al.[76]) and is in good agreement with the global-average vertical distribution in the results of McErlich et al.[25] (shown in Fig. 4a). We denote this distribution by 'whole troposphere'.

$$\rho(z) = \rho_0 \times \begin{cases} 1 & z \le z_{\text{BL}} \\ 0.3^{(z-z_{\text{BL}})/10\text{ km}} & z_{\text{BL}} < z \le z_{\text{trop}} \\ 0 & z > z_{\text{trop}} \end{cases} \tag{11}$$

where z_{trop} is the monthly-mean tropopause height taken from the control HadGEM3-GA7.1 simulation. We set $z_{\text{BL}} = 2$ km as an approximation to the depth of the planetary boundary layer (PBL). Both vertical distributions are shown in Fig. 4a.

The assumption of a constant PBL height $z_{\text{BL}} = 2$ km (see Section 4.3 and Equation 11) is not a good approximation to reality, where the PBL varies in depth between $\sim$ 500 m and $\sim$ 3 km depending on season, land surface, and local atmospheric conditions[77,78]. However, variations in the value of z_{BL} only negligibly affect our IRF results (Supplementary Fig. S3 and accompanying text).

Acknowledgements

This research was supported by the Royal Society Te Apārangi Marsden Fund (contracts 22-UOC-088 and VUW-2118) and Rutherford Discovery Fellowships (22-UOC-14), administered by the Royal Society Te Apārangi. N.E. was supported by the Norwegian Research Council (NFR) project MAGIC (Airborne Microplastic Detection, Origin, Transport and Global Radiative Impact, Project No.: 334086). We acknowledge the UK Met Office for the use of HadGEM3-GA7.1 and SOCRATES. The authors wish to acknowledge use of the eResearch Infrastructure Platform hosted by the Crown company, Research and Education Advanced Network New Zealand (REANNZ) Ltd., and funded by the Ministry of Business, Innovation & Employment: `https://www.reannz.co.nz`.

References

[1] X. Zhao, Y. Zhou, C. Liang, J. Song, S. Yu, G. Liao, P. Zou, K. H. D. Tang, and C. Wu. Airborne microplastics: Occurrence, sources, fate, risks and mitigation. *Science of The Total Environment*, 858:159943, February 2023. ISSN 0048-9697. doi: 10.1016/j.scitotenv.2022.159943.

[2] D. Allen, S. Allen, S. Abbasi, A. Baker, M. Bergmann, J. Brahney, T. Butler, R. A. Duce, S. Eckhardt, N. Evangeliou, T. Jickells, M. Kanakidou, P. Kershaw, P. Laj, J. Levermore, D. Li, P. Liss, K. Liu, N. Mahowald, P. Masque, D. Materić, A. G. Mayes, P. McGinnity, I. Osvath, K. A. Prather, J. M. Prospero, L. E. Revell, S. G. Sander, W. J. Shim, J. Slade, A. Stein, O. Tarasova, and S. Wright. Microplastics and nanoplastics in the marine-atmosphere environment. *Nature Reviews Earth & Environment*, 3(6):393–405, June 2022. ISSN 2662-138X. doi: 10.1038/s43017-022-00292-x.

[3] N. Evangeliou, H. Grythe, Z. Klimont, C. Heyes, S. Eckhardt, S. Lopez-Aparicio, and A. Stohl. Atmospheric transport is a major pathway of microplastics to remote regions. *Nature Communications*, 11(1):3381, July 2020. ISSN 2041-1723. doi: 10.1038/s41467-020-17201-9.

[4] S. Allen, D. Allen, V. R. Phoenix, G. Le Roux, P. Durántez Jiménez, A. Simonneau, S. Binet, and D. Galop. Atmospheric transport and deposition of microplastics in a remote mountain catchment. *Nature Geoscience*, 12(5):339–344, May 2019. ISSN 1752-0894, 1752-0908. doi: 10.1038/s41561-019-0335-5.

[5] Q. Chen, G. Shi, L. E. Revell, J. Zhang, C. Zuo, D. Wang, E. C. Le Ru, G. Wu, and D. M. Mitrano. Long-range atmospheric transport of microplastics across the southern hemisphere. *Nature Communications*, 14(1):7898, November 2023. ISSN 2041-1723. doi: 10.1038/s41467-023-43695-0.

[6] J. E. Sonke, A. M. Koenig, N. Yakovenko, O. Hagelskjær, H. Margenat, S. V. Hansson, F. De Vleeschouwer, O. Magand, G. Le Roux, and J. L. Thomas. A mass budget and box model of global plastics cycling, degradation and dispersal in the land-ocean-atmosphere system. *Microplastics and Nanoplastics*, 2(1):28, December 2022. ISSN 2662-4966. doi: 10.1186/s43591-022-00048-w.

[7] J.-L. Xu, X. Lin, J. J. Wang, and A. A. Gowen. A review of potential human health impacts of micro- and nanoplastics exposure. *Science of The Total Environment*, 851:158111, December 2022. ISSN 0048-9697. doi: 10.1016/j.scitotenv.2022.158111.

[8] S. Twomey. The Influence of Pollution on the Shortwave Albedo of Clouds. *Journal of the Atmospheric Sciences*, July 1977. ISSN 1520-0469.

[9] B. A. Albrecht. Aerosols, Cloud Microphysics, and Fractional Cloudiness. *Science*, 245 (4923):1227–1230, September 1989. doi: 10.1126/science.245.4923.1227.

[10] M. Aeschlimann, G. Li, Z. A. Kanji, and D. M. Mitrano. Potential impacts of atmospheric microplastics and nanoplastics on cloud formation processes. *Nature Geoscience*, 15(12): 967–975, December 2022. ISSN 1752-0894, 1752-0908. doi: 10.1038/s41561-022-01051-9.

[11] M. Ganguly and P. A. Ariya. Ice Nucleation of Model Nanoplastics and Microplastics: A Novel Synthetic Protocol and the Influence of Particle Capping at Diverse Atmospheric Environments. *ACS Earth and Space Chemistry*, 3(9):1729–1739, September 2019. doi: 10.1021/acsearthspacechem.9b00132. Publisher: American Chemical Society.

[12] T. M. Seifried, S. Nikkho, A. Morales Murillo, L. J. Andrew, E. R. Grant, and A. K. Bertram. Microplastic particles contain ice nucleation sites that can be deactivated by atmospheric aging, March 2024.

[13] D. Tatsii, B. Gasparini, I. Evangelou, S. Bucci, and A. Stohl. Do Microplastics Contribute to the Total Number Concentration of Ice Nucleating Particles? *Journal of Geophysical Research: Atmospheres*, 130(2):e2024JD042827, 2025. ISSN 2169-8996. doi: 10.1029/2024JD042827.

[14] R. L. Reynolds, N. Molden, R. F. Kokaly, H. Lowers, G. N. Breit, H. L. Goldstein, E. K. Williams, C. R. Lawrence, and J. Derry. Microplastic and Associated Black Particles From Road-Tire Wear: Implications for Radiative Effects Across the Cryosphere and in the Atmosphere. *Journal of Geophysical Research: Atmospheres*, 129(19):e2024JD041116, 2024. ISSN 2169-8996. doi: 10.1029/2024JD041116.

[15] J. Ming and F. Wang. Microplastics' Hidden Contribution to Snow Melting. https://eos.org/opinions/microplastics-hidden-contribution-to-snow-melting, March 2021.

[16] L. E. Revell, P. Kuma, E. C. Le Ru, W. R. C. Somerville, and S. Gaw. Direct radiative effects of airborne microplastics. *Nature*, 598(7881):462–467, October 2021. ISSN 0028-0836, 1476-4687. doi: 10.1038/s41586-021-03864-x.

[17] H. Yang, Y. Xue, X. Sha, J. Yang, X. Wang, B. Suvdantsetseg, K. Kuroda, J. Pu, and L. Wang. Influence of regional environmental variables on the radiative forcing of atmospheric microplastics. *Eco-Environment & Health*, 4(1):100128, March 2025. ISSN 27729850. doi: 10.1016/j.eehl.2024.11.002.

[18] Q. Pang, X. Wang, B. Zhuang, H. Wang, and Y. Zhang. A Model-based Estimate for the Direct Radiative Effect of Atmospheric Microplastics. *Atmospheric Environment*, page 121305, May 2025. ISSN 1352-2310. doi: 10.1016/j.atmosenv.2025.121305.

[19] Y. Liu, H. Fu, H. Zhang, Y. Wang, R. K. Chakrabarty, X. Tu, X. Tang, A. Laskin, G. R. Carmichael, J. Chen, J. S. Francisco, and D. T. Shindell. Atmospheric warming contributions from airborne microplastics and nanoplastics. *Nature Climate Change*, pages 1–8, May 2026. ISSN 1758-6798. doi: 10.1038/s41558-026-02620-1.

[20] O. Mbachu, G. Jenkins, C. Pratt, and P. Kaparaju. A New Contaminant Superhighway? A Review of Sources, Measurement Techniques and Fate of Atmospheric Microplastics. *Water, Air, & Soil Pollution*, 231(2):85, February 2020. ISSN 0049-6979, 1573-2932. doi: 10.1007/s11270-020-4459-4.

[21] L. Shao, Y. Li, T. Jones, M. Santosh, P. Liu, M. Zhang, L. Xu, W. Li, J. Lu, C.-X. Yang, D. Zhang, X. Feng, and K. BéruBé. Airborne microplastics: A review of current perspectives and environmental implications. *Journal of Cleaner Production*, 347:131048, May 2022. ISSN 0959-6526. doi: 10.1016/j.jclepro.2022.131048.

[22] F. D. Leusch, H.-C. Lu, K. Perera, P. A. Neale, and S. Ziajahromi. Analysis of the literature shows a remarkably consistent relationship between size and abundance of microplastics across different environmental matrices. *Environmental Pollution*, 319:120984, February 2023. ISSN 02697491. doi: 10.1016/j.envpol.2022.120984.

[23] D. Tatsii, S. Bucci, T. Bhowmick, J. Guettler, L. Bakels, G. Bagheri, and A. Stohl. Shape Matters: Long-Range Transport of Microplastic Fibers in the Atmosphere. *Environmental Science & Technology*, 58(1):671–682, January 2024. ISSN 0013-936X, 1520-5851. doi: 10.1021/acs.est.3c08209.

[24] S. Bucci, C. Richon, and L. Bakels. Exploring the Transport Path of Oceanic Microplastics in the Atmosphere. *Environmental Science & Technology*, 58(32):14338–14347, August 2024. ISSN 0013-936X, 1520-5851. doi: 10.1021/acs.est.4c03216.

[25] C. McErlich, F. Goddard, A. Aves, C. Hardacre, N. Evangeliou, A. J. Hewitt, and L. E. Revell. Description and evaluation of airborne microplastics in the United Kingdom Earth System Model (UKESM1.1) using GLOMAP-mode. *Geoscientific Model Development*, 18 (22):8827–8854, November 2025. ISSN 1991-959X. doi: 10.5194/gmd-18-8827-2025.

[26] G. Myhre, B. H. Samset, M. Schulz, Y. Balkanski, S. Bauer, T. K. Berntsen, H. Bian, N. Bellouin, M. Chin, T. Diehl, R. C. Easter, J. Feichter, S. J. Ghan, D. Hauglustaine, T. Iversen, S. Kinne, A. Kirkevåg, J.-F. Lamarque, G. Lin, X. Liu, M. T. Lund, G. Luo, X. Ma, T. van Noije, J. E. Penner, P. J. Rasch, A. Ruiz, Ø. Seland, R. B. Skeie, P. Stier, T. Takemura, K. Tsigaridis, P. Wang, Z. Wang, L. Xu, H. Yu, F. Yu, J.-H. Yoon, K. Zhang, H. Zhang, and C. Zhou. Radiative forcing of the direct aerosol effect from AeroCom Phase II simulations. *Atmospheric Chemistry and Physics*, 13(4):1853–1877, February 2013. ISSN 1680-7316. doi: 10.5194/acp-13-1853-2013.

[27] X. Liu, J. E. Penner, and M. Herzog. Global modeling of aerosol dynamics: Model description, evaluation, and interactions between sulfate and nonsulfate aerosols. *Journal of Geophysical Research: Atmospheres*, 110(D18):2004JD005674, 2005. doi: 10.1029/2004JD005674.

[28] X. Ma and K. Von Salzen. Dynamics of the sulphate aerosol size distribution on a global scale. 111:2005JD006620, April 2006. doi: 10.1029/2005JD006620.

[29] Á. Mészáros. On the size distribution of atmospheric aerosol particles of different composition. *Atmospheric Environment (1967)*, 11(11):1075–1081, January 1977. ISSN 00046981. doi: 10.1016/0004-6981(77)90237-2.

[30] G. D. Thornhill, W. J. Collins, R. J. Kramer, D. Olivié, R. B. Skeie, F. M. O'Connor, N. L. Abraham, R. Checa-Garcia, S. E. Bauer, M. Deushi, L. K. Emmons, P. M. Forster, L. W. Horowitz, B. Johnson, J. Keeble, J.-F. Lamarque, M. Michou, M. J. Mills, J. P. Mulcahy, G. Myhre, P. Nabat, V. Naik, N. Oshima, M. Schulz, C. J. Smith, T. Takemura, S. Tilmes, T. Wu, G. Zeng, and J. Zhang. Effective radiative forcing from emissions of reactive gases and aerosols – a multi-model comparison. *Atmospheric Chemistry and Physics*, 21(2):853–874, January 2021. ISSN 1680-7316. doi: 10.5194/acp-21-853-2021.

[31] H. Wiesinger, Z. Wang, and S. Hellweg. Deep Dive into Plastic Monomers, Additives, and Processing Aids. *Environmental Science & Technology*, 55(13):9339–9351, July 2021. ISSN 0013-936X. doi: 10.1021/acs.est.1c00976.

[32] T. Grigoratos and G. Martini. Brake wear particle emissions: A review. *Environmental Science and Pollution Research*, 22(4):2491–2504, February 2015. ISSN 0944-1344, 1614-7499. doi: 10.1007/s11356-014-3696-8.

[33] M. Bergmann, S. Mützel, S. Primpke, M. B. Tekman, J. Trachsel, and G. Gerdts. White and wonderful? Microplastics prevail in snow from the Alps to the Arctic. *Science Advances*, 5(8):eaax1157, August 2019. ISSN 2375-2548. doi: 10.1126/sciadv.aax1157.

[34] S. Abbasi, M. Alirezazadeh, N. Razeghi, M. Rezaei, H. Pourmahmood, R. Dehbandi, M. R. Mehr, S. Y. Ashayeri, P. Oleszczuk, and A. Turner. Microplastics captured by snowfall: A study in Northern Iran. *Science of The Total Environment*, 822:153451, May 2022. ISSN 0048-9697. doi: 10.1016/j.scitotenv.2022.153451.

[35] S. Kang, Y. Zhang, Y. Qian, and H. Wang. A review of black carbon in snow and ice and its impact on the cryosphere. *Earth-Science Reviews*, 210:103346, November 2020. ISSN 0012-8252. doi: 10.1016/j.earscirev.2020.103346.

[36] M. Kooi and A. A. Koelmans. Simplifying Microplastic via Continuous Probability Distributions for Size, Shape, and Density. *Environmental Science & Technology Letters*, 6(9): 551–557, September 2019. ISSN 2328-8930, 2328-8930. doi: 10.1021/acs.estlett.9b00379.

[37] L. Wang, P. Li, Q. Zhang, W.-M. Wu, J. Luo, and D. Hou. Modeling the Conditional Fragmentation-Induced Microplastic Distribution. *Environmental Science & Technology*, 55(9):6012–6021, May 2021. ISSN 0013-936X, 1520-5851. doi: 10.1021/acs.est.1c01042.

[38] G. Chen, Z. Fu, H. Yang, and J. Wang. An overview of analytical methods for detecting microplastics in the atmosphere. *TrAC Trends in Analytical Chemistry*, 130:115981, September 2020. ISSN 0165-9936. doi: 10.1016/j.trac.2020.115981.

[39] D. Materić, A. Kasper-Giebl, D. Kau, M. Anten, M. Greilinger, E. Ludewig, E. van Sebille, T. Röckmann, and R. Holzinger. Micro- and Nanoplastics in Alpine Snow: A New Method for Chemical Identification and (Semi)Quantification in the Nanogram Range. *Environmental Science & Technology*, 54(4):2353–2359, February 2020. ISSN 0013-936X. doi: 10.1021/acs.est.9b07540.

[40] A. Aves, A. MacDonald, S. Naeher, D. Materić, D. Castle, P. Davy, S. Gaw, and L. E. Revell. Comparative assessment of five analytical methods for airborne microplastics highlights importance of identifying sub- $$10~\upmu \hbox {m}$$ methods. *Scientific Reports*, May 2026. doi: 10.1038/s41598-026-49405-2. URL `https://www.nature.com/articles/s41598-026-49405-2`.

[41] B. H. Samset and G. Myhre. Vertical dependence of black carbon, sulphate and biomass burning aerosol radiative forcing. *Geophysical Research Letters*, 38(24), 2011. ISSN 1944-8007. doi: 10.1029/2011GL049697.

[42] S. K. Satheesh, V. Vinoj, and K. K. Moorthy. Vertical distribution of aerosols over an urban continental site in India inferred using a micro pulse lidar. *Geophysical Research Letters*, 33(20):2006GL027729, October 2006. ISSN 0094-8276, 1944-8007. doi: 10.1029/2006GL027729.

[43] B. Koffi, M. Schulz, F.-M. Bréon, J. Griesfeller, D. Winker, Y. Balkanski, S. Bauer, T. Berntsen, M. Chin, W. D. Collins, F. Dentener, T. Diehl, R. Easter, S. Ghan, P. Ginoux, S. Gong, L. W. Horowitz, T. Iversen, A. Kirkevåg, D. Koch, M. Krol, G. Myhre, P. Stier, and T. Takemura. Application of the CALIOP layer product to evaluate the vertical distribution of aerosols estimated by global models: AeroCom phase I results. *Journal of Geophysical Research: Atmospheres*, 117(D10):2011JD016858, May 2012. ISSN 0148-0227. doi: 10.1029/2011JD016858.

[44] Q. Zhang, X. Ma, X. Tie, M. Huang, and C. Zhao. Vertical distributions of aerosols under different weather conditions: Analysis of in-situ aircraft measurements in Beijing, China. *Atmospheric Environment*, 43(34):5526–5535, November 2009. ISSN 1352-2310. doi: 10.1016/j.atmosenv.2009.05.037.

[45] X. Sun, Y. Yin, Y. Sun, Y. Sun, W. Liu, and Y. Han. Seasonal and vertical variations in aerosol distribution over Shijiazhuang, China. *Atmospheric Environment*, 81:245–252, December 2013. ISSN 1352-2310. doi: 10.1016/j.atmosenv.2013.08.009.

[46] S. Sridharan, M. Kumar, L. Singh, N. S. Bolan, and M. Saha. Microplastics as an emerging source of particulate air pollution: A critical review. *Journal of Hazardous Materials*, 418: 126245, September 2021. ISSN 0304-3894. doi: 10.1016/j.jhazmat.2021.126245.

[47] B. Gewert, M. M. Plassmann, and M. MacLeod. Pathways for degradation of plastic polymers floating in the marine environment. *Environmental Science: Processes & Impacts*, 17 (9):1513–1521, 2015. doi: 10.1039/C5EM00207A.

[48] A. Chamas, H. Moon, J. Zheng, Y. Qiu, T. Tabassum, J. H. Jang, M. Abu-Omar, S. L. Scott, and S. Suh. Degradation Rates of Plastics in the Environment. *ACS Sustainable Chemistry & Engineering*, 8(9):3494–3511, March 2020. doi: 10.1021/acssuschemeng.9b06635.

[49] S. Allen, D. Allen, K. Moss, G. L. Roux, V. R. Phoenix, and J. E. Sonke. Examination of the ocean as a source for atmospheric microplastics. *PLOS ONE*, 15(5):e0232746, May 2020. ISSN 1932-6203. doi: 10.1371/journal.pone.0232746.

[50] C. Harb, N. Pokhrel, and H. Foroutan. Quantification of the Emission of Atmospheric Microplastics and Nanoplastics via Sea Spray. *Environmental Science & Technology Letters*, 10(6):513–519, June 2023. ISSN 2328-8930, 2328-8930. doi: 10.1021/acs.estlett.3c00164.

[51] D. B. Shaw, Q. Li, J. K. Nunes, and L. Deike. Ocean emission of microplastic. *PNAS Nexus*, 2(10):pgad296, September 2023. ISSN 2752-6542. doi: 10.1093/pnasnexus/pgad296.

[52] X. Wang, N. Wei, K. Liu, L. Zhu, C. Li, C. Zong, and D. Li. Exponential decrease of airborne microplastics: From megacity to open ocean. *Science of The Total Environment*, 849: 157702, November 2022. ISSN 0048-9697. doi: 10.1016/j.scitotenv.2022.157702.

[53] S. Yang, X. Lu, and X. Wang. A Perspective on the Controversy over Global Emission Fluxes of Microplastics from Ocean into the Atmosphere. *Environmental Science & Technology*, 58(28):12304–12312, July 2024. ISSN 0013-936X. doi: 10.1021/acs.est.4c03182.

[54] S. Yang, T. Zhang, Y. Gan, X. Lu, H. Chen, J. Chen, X. Yang, and X. Wang. Constraining Microplastic Particle Emission Flux from the Ocean. *Environmental Science & Technology Letters*, 9(6):513–519, June 2022. ISSN 2328-8930, 2328-8930. doi: 10.1021/acs.estlett.2c00214.

[55] S. Yang, G. Brasseur, S. Walters, P. Lichtig, and C. W. Y. Li. Global atmospheric distribution of microplastics with evidence of low oceanic emissions. *npj Climate and Atmospheric Science*, 8(1):1–10, February 2025. ISSN 2397-3722. doi: 10.1038/s41612-025-00914-3.

[56] I. Evangelou, S. Bucci, and A. Stohl. Atmospheric microplastic emissions from land and ocean. *Nature*, pages 1–4, January 2026. ISSN 1476-4687. doi: 10.1038/s41586-025-09998-6.

[57] M. Zhang, H. Yin, J. Tan, X. Wang, Z. Yang, L. Hao, T. Du, Z. Niu, and Y. Ge. A comprehensive review of tyre wear particles: Formation, measurements, properties, and influencing factors. *Atmospheric Environment*, 297:119597, March 2023. ISSN 13522310. doi: 10.1016/j.atmosenv.2023.119597.

[58] F. Dentener, B. Hall, and C. Smith. Annex III: Tables of historical and projected well-mixed greenhouse gas mixing ratios and effective radiative forcing of all climate forcers. In V. Masson-Delmotte, P. Zhai, A. Pirani, S. Connors, C. Péan, S. Berger, N. Caud, Y. Chen, L. Goldfarb, M. Gomis, M. Huang, K. Leitzell, E. Lonnoy, J. Matthews, T. Maycock, T. Waterfield, O. Yelekçi, R. Yu, and B. Zhou, editors, *Climate Change 2021: The Physical Science Basis*, pages 2139–2152. Cambridge University Press, Cambridge, United Kingdom and New York, NY, USA, 2021. doi: 10.1017/9781009157896.017.

[59] P. Stegmann, V. Daioglou, M. Londo, D. P. van Vuuren, and M. Junginger. Plastic futures and their CO2 emissions. *Nature*, 612(7939):272–276, December 2022. ISSN 1476-4687. doi: 10.1038/s41586-022-05422-5.

[60] P. Forster, K. Armour, W. Collins, J.-L. Dufresne, D. Frame, D. J. Lunt, T. Mauritsen, M. D. Palmer, M. Watanabe, M. Wild, and H. Zhang. The Earth's Energy Budget, Climate Feedbacks, and Climate Sensitivity. In V. Masson-Delmotte, P. Zhai, A. Pirani, S. L. Connors, C. Péan, S. Berger, N. Caud, Y. Chen, L. Goldfarb, M. I. Gomis, M. Huang, K. Leitzell, E. Lonnoy, J. B. R. Matthews, T. K. Maycock, T. Waterfield, O. Yelekçi, R. Yu, and B. Zhou, editors, *Climate Change 2021: The Physical Science Basis. Contribution of Working Group I to the Sixth Assessment Report of the Intergovernmental Panel on Climate Change*, pages 923–1054. Cambridge University Press, Cambridge, United Kingdom and New York, NY, USA, 2021.

[61] P. M. Forster, T. Richardson, A. C. Maycock, C. J. Smith, B. H. Samset, G. Myhre, T. Andrews, R. Pincus, and M. Schulz. Recommendations for diagnosing effective radiative forcing from climate models for CMIP6. *Journal of Geophysical Research: Atmospheres*, 121(20):12,460–12,475, 2016. ISSN 2169-8996. doi: 10.1002/2016JD025320. _eprint: https://onlinelibrary.wiley.com/doi/pdf/10.1002/2016JD025320.

[62] S. C. Sherwood, S. Bony, O. Boucher, C. Bretherton, P. M. Forster, J. M. Gregory, and B. Stevens. Adjustments in the Forcing-Feedback Framework for Understanding Climate Change. *Bulletin of the American Meteorological Society*, 96(2):217–228, February 2015. ISSN 0003-0007, 1520-0477. doi: 10.1175/BAMS-D-13-00167.1.

[63] O. Boucher, D. Randall, P. Artaxo, C. Bretherton, G. Feingold, P. Forster, V.-M. Kerminen, Y. Kondo, H. Liao, U. Lohmann, P. Rasch, S. K. Satheesh, S. Sherwood, B. Stevens, and X. Y. Zhang. Clouds and Aerosols. In T. F. Stocker, D. Qin, G.-K. Plattner, M. Tignor, S. K. Allen, J. Boschung, A. Nauels, Y. Xia, V. Bex, and P. M. Midgley, editors, *Climate Change 2013: The Physical Science Basis. Contribution of Working Group I to the Fifth Assessment Report of the Intergovernmental Panel on Climate Change*, pages 571–657. Cambridge University Press, Cambridge, United Kingdom and New York, NY, USA, 2013.

[64] Y. Wang, H. Okochi, Y. Tani, H. Hayami, Y. Minami, N. Katsumi, M. Takeuchi, A. Sorimachi, Y. Fujii, M. Kajino, K. Adachi, Y. Ishihara, Y. Iwamoto, and Y. Niida. Airborne hydrophilic microplastics in cloud water at high altitudes and their role in cloud formation. *Environmental Chemistry Letters*, 21(6):3055–3062, December 2023. ISSN 1610-3661. doi: 10.1007/s10311-023-01626-x.

[65] D. Walters, A. J. Baran, I. Boutle, M. Brooks, P. Earnshaw, J. Edwards, K. Furtado, P. Hill, A. Lock, J. Manners, C. Morcrette, J. Mulcahy, C. Sanchez, C. Smith, R. Stratton, W. Tennant, L. Tomassini, K. Van Weverberg, S. Vosper, M. Willett, J. Browse, A. Bushell, K. Carslaw, M. Dalvi, R. Essery, N. Gedney, S. Hardiman, B. Johnson, C. Johnson, A. Jones, C. Jones, G. Mann, S. Milton, H. Rumbold, A. Sellar, M. Ujiie, M. Whitall, K. Williams, and M. Zerroukat. The Met Office Unified Model Global Atmosphere 7.0/7.1 and JULES Global Land 7.0 configurations. *Geoscientific Model Development*, 12(5):1909–1963, May 2019. ISSN 1991-959X. doi: 10.5194/gmd-12-1909-2019. Publisher: Copernicus GmbH.

[66] J. M. Edwards and A. Slingo. Studies with a flexible new radiation code. I: Choosing a configuration for a large-scale model. *Quarterly Journal of the Royal Meteorological Society*, 122(531):689–719, 1996. ISSN 1477-870X. doi: 10.1002/qj.49712253107.

[67] H. A. Titchner and N. A. Rayner. The Met Office Hadley Centre sea ice and sea surface temperature data set, version 2: 1. Sea ice concentrations. *Journal of Geophysical Research: Atmospheres*, 119(6):2864–2889, 2014. ISSN 2169-8996. doi: 10.1002/2013JD020316. _eprint: https://onlinelibrary.wiley.com/doi/pdf/10.1002/2013JD020316.

[68] J.-F. Lamarque, T. C. Bond, V. Eyring, C. Granier, A. Heil, Z. Klimont, D. Lee, C. Liousse, A. Mieville, B. Owen, M. G. Schultz, D. Shindell, S. J. Smith, E. Stehfest, J. Van Aardenne, O. R. Cooper, M. Kainuma, N. Mahowald, J. R. McConnell, V. Naik,

K. Riahi, and D. P. van Vuuren. Historical (1850–2000) gridded anthropogenic and biomass burning emissions of reactive gases and aerosols: methodology and application. *Atmospheric Chemistry and Physics*, 10(15):7017–7039, August 2010. ISSN 1680-7316. doi: 10.5194/acp-10-7017-2010. Publisher: Copernicus GmbH.

[69] J. L. Lean and M. T. DeLand. How Does the Sun's Spectrum Vary? April 2012. doi: 10.1175/JCLI-D-11-00571.1. Section: Journal of Climate.

[70] H. Hersbach, B. Bell, P. Berrisford, S. Hirahara, A. Horányi, J. Muñoz-Sabater, J. Nicolas, C. Peubey, R. Radu, D. Schepers, A. Simmons, C. Soci, S. Abdalla, X. Abellan, G. Balsamo, P. Bechtold, G. Biavati, J. Bidlot, M. Bonavita, G. De Chiara, P. Dahlgren, D. Dee, M. Diamantakis, R. Dragani, J. Flemming, R. Forbes, M. Fuentes, A. Geer, L. Haimberger, S. Healy, R. J. Hogan, E. Hólm, M. Janisková, S. Keeley, P. Laloyaux, P. Lopez, C. Lupu, G. Radnoti, P. de Rosnay, I. Rozum, F. Vamborg, S. Villaume, and J.-N. Thépaut. The ERA5 global reanalysis. *Quarterly Journal of the Royal Meteorological Society*, 146(730): 1999–2049, 2020. ISSN 1477-870X. doi: 10.1002/qj.3803.

[71] I. Ouchi. Anisotropic Absorption and Reflection Spectra of Poly(ethylene terephthalate) Films in Ultraviolet Region. *Polymer Journal*, 15(3):225–243, March 1983. ISSN 1349-0540. doi: 10.1295/polymj.15.225.

[72] A. Djorović, M. Meyer, B. L. Darby, and E. C. Le Ru. Accurate Modeling of the Polarizability of Dyes for Electromagnetic Calculations. *ACS Omega*, 2(5):1804–1811, May 2017. doi: 10.1021/acsomega.7b00171.

[73] N. Evangeliou, O. Tichý, S. Eckhardt, C. G. Zwaaftink, and J. Brahney. Sources and fate of atmospheric microplastics revealed from inverse and dispersion modelling: From global emissions to deposition. *Journal of Hazardous Materials*, 432:128585, 2022. ISSN 0304-3894. doi: https://doi.org/10.1016/j.jhazmat.2022.128585.

[74] A. Isobe, T. Azuma, M. R. Cordova, A. Cózar, F. Galgani, R. Hagita, L. D. Kanhai, K. Imai, S. Iwasaki, S. Kako, N. Kozlovskii, A. L. Lusher, S. A. Mason, Y. Michida, T. Mituhasi, Y. Morii, T. Mukai, A. Popova, K. Shimizu, T. Tokai, K. Uchida, M. Yagi, and W. Zhang. A multilevel dataset of microplastic abundance in the world's upper ocean and the Laurentian Great Lakes. *Microplastics and Nanoplastics*, 1(1):16, September 2021. ISSN 2662-4966. doi: 10.1186/s43591-021-00013-z.

[75] Y. Xiang, T. Zhang, J. Liu, X. Wan, M. Loewen, X. Chen, S. Kang, Y. Fu, L. Lv, W. Liu, and Z. Cong. Vertical profile of aerosols in the Himalayas revealed by lidar: New insights into their seasonal/diurnal patterns, sources, and transport. *Environmental Pollution*, 285: 117686, September 2021. ISSN 0269-7491. doi: 10.1016/j.envpol.2021.117686.

[76] P. J. Sheridan, E. Andrews, J. A. Ogren, J. L. Tackett, and D. M. Winker. Vertical profiles of aerosol optical properties over central Illinois and comparison with surface and satellite measurements. *Atmospheric Chemistry and Physics*, 12(23):11695–11721, December 2012. ISSN 1680-7316. doi: 10.5194/acp-12-11695-2012.

[77] E. L. McGrath-Spangler and A. S. Denning. Global seasonal variations of midday planetary boundary layer depth from CALIPSO space-borne LIDAR. *Journal of Geophysical Research: Atmospheres*, 118(3):1226–1233, 2013. ISSN 2169-8996. doi: 10.1002/jgrd.50198.

[78] K. M. Chan and R. Wood. The seasonal cycle of planetary boundary layer depth determined using COSMIC radio occultation data. *Journal of Geophysical Research: Atmospheres*, 118(22):12,422–12,434, 2013. ISSN 2169-8996. doi: 10.1002/2013JD020147.

Supplementary Files

This is a list of supplementary files associated with this preprint. Click to download.

- SUPPLEMENTARY.pdf